

Machine Learning for Sideband Detection in Free-Electron Laser

Kelley P Valentine, Guanqun Zhou, and Juhao Wu

Abstract

Free-Electron Laser (FEL) sideband instability can have negative consequences, such as degrading spectral purity or limiting FEL power. As such, we must identify and better understand sideband so we might learn to suppress it. However, because FEL sideband is far from the main signal, it is very weak and can hardly be detected from background noise. Therefore, we created software that uses Machine Learning, specifically the mean shift algorithm (Cheng, 1995), to detect such sideband. The software is written in Python 3.7.0 and is available for public distribution on GitHub (Valentine, 2018).

1 Introduction

A Free-Electron Laser (FEL) is perceived as the fourth-generation synchrotron light source, capable of generating coherent high-power radiation over a broad spectrum from far infrared to hard X-rays. Of particular interest is the atomic wavelength regime, *e.g.* from a fraction of a nanometer down to tenths of an angstrom, where the applications (Emma, et al., 2010) (Ishikawa, et al., 2012) (Aquila, et al., 2015) typically require the radiation power in the hard X-ray regime with peak power in the terawatt (TW) range.

In a high-gain FEL, the main signal, which originates from the resonance condition, grows exponentially until saturation occurs. This saturation is normally referred to as the first saturation. For the case of a constant or untapered undulator, the radiation power oscillates around equilibrium after the first saturation point. In the X-ray FEL regime, the power efficiency (defined as the ratio of the FEL radiation power to the electron beam power) is about 10^{-3} , indicating that the output peak power can be ~ 50 GW for an electron beam with peak current ~ 5 kA and energy ~ 10 GeV operating in the self-amplified spontaneous emission (SASE) mode in a ~ 100 -m-long untapered undulator. Though undulator tapering had been proposed since the 1980s, recently there have been renewed interests in tapering to achieve enhanced energy conversion efficiency, improved spectral purity, or for polarization control (see, for example, Refs. (Kroll, Morton, & Rosenbluth, 1981) (Jiao, et al, 2012) (Emma, Fang, Wu, & Pellegrini, 2016) (Wu, et al., 2017) (Geloni, Kocharyan, & Saldin, 2011) (Schneidmiller & Yurkov, 2013) (Tsai, Wu, Yang, Yoon & Zhou, 2017) (Tsai, Wu, Yang, Yoon, & Zhou, 2018)). With undulator tapering, the efficiency can be improved and the power can be further increased in the post-first-saturation regime (however, at a lower rate compared with the exponential growth in the linear regime) but eventually will reach a so-called second saturation and the radiation then approaches another equilibrium. Although numerical simulations show that TW-level FEL output power can

be possible when undulator tapering is optimized and the combined SASE and self-seeded scheme is employed (see, for example, Ref. (Emma, Fang Wu, & Pellegrini, 2016)), in the post-first-saturation regime it is the sideband instability that still limits the growth of the main signal (Kroll, Morton, & Rosenbluth, 1981) (Davidson & Wurtele, 1987) (Sharp & Yu, 1990) (Pilla & Bhattacharjee, 1994) (Riyopoulos, 2000); and hence leads to the second-saturation. Enhancing the FEL peak power shall be envisioned once the sideband instability can be effectively suppressed.

The sideband instability in an FEL is caused by the interaction of the electromagnetic field with the electron synchrotron motion in the ponderomotive potential well. Such a potential well, formed by the undulator magnetic field and the main signal, will trap electrons and result in the oscillation with a synchrotron frequency (and its multiples) away from the resonance frequency (*i.e.* the frequency of the main signal). Once the interaction creates a positive feedback, the electron beam energy will transfer and contribute to the electromagnetic field with the synchrotron sideband frequency outside of the main signal bandwidth. The sideband signal will continue to grow and usually cause undesirable consequences. For example, it can degrade the spectral purity and may limit the level of the final FEL power at the second saturation (Emma, Fang, Wu, & Pellegrini, 2016).

The early study of FEL sideband instability can be traced back to the 1980s (Kroll, Morton, & Rosenbluth, 1981) (Davidson & Wurtele, 1987). The stability analyses are usually treated by single-particle or kinetic methods. Both approaches may assume small perturbations of electron synchrotron motion and radiation fields from the equilibria. While they may provide practical use to quickly estimate whether the sideband instability will be an issue, most of the previous work assumes constant-parameter undulators (Kroll, Morton, & Rosenbluth, 1981) (Davidson & Wurtele, 1987) (Sharp & Yu, 1990), focuses on longer wavelength regime (Pilla & Bhattacharjee, 1994) (Masud, et al., 1987) (Yee, Masud, Marshall, & Schlesinger, 1987), or addresses oscillator configurations (Tokar, McVey, & Goldstein, 1988) (Quimby, 1988). Recently Lindberg (Lindberg, 2015) and Zhang *et al.* (Zhang, et al., 2016) have theoretically investigated the FEL sideband instability induced by initial beam modulations, in which their studies focus on a mechanism in the linear or exponential regime with a constant undulator parameter. Thereafter the beam-modulation induced sidebands have been intensively studied with numerical (Hemsing, Garcia, Huang, Raubenheimer, & Xiang, 2017) (Ribic, et al. 2017) and experimental (Roussel, et al., 2015) studies. We remind that their studies assume the sideband signal lies within the typical FEL SASE gain bandwidth. Therefore, both the main and sideband signals are exponentially amplified in the linear regime.

Given these renewed interests, we conducted extensive studies both theoretically (Tsai, Wu, Yang, Yoon, & Zhou, 2017) (Tsai, Wu, Yang, Yoon, & Zhou, 2018) and experimentally. In our theoretical study, we follow the notations of Bonifacio *et al.* (Bonifacio, Casagrande, Ferrario, Pierini, & Piovela, 1988) and Isermann and Graham (Isermann & Graham, 1992). Our work (Tsai, Wu, Yang, Yoon, & Zhou, 2017) (Tsai, Wu, Yang, Yoon, & Zhou, 2018) differs from the work above

mentioned (Lindberg, 2015) (Zhang, et al., 2016) (Hemsing, Garcia, Huang, Raubenheimer, & Xiang, 2017) (Ribic, et al., 2017) (Roussel, et al., 2015) in that we study sideband instability outside of the main signal SASE bandwidth. Because such sideband signals are far away from the main signal, the sideband signal strength is very weak.

Encouraged by the positive theoretical study results (Tsai, Wu, Yang, Yoon, & Zhou, 2017) (Tsai, Wu, Yang, Yoon, & Zhou, 2018), we conducted experiments on the LINAC Coherent Light Source (Emma, et al., 2010). As mentioned above, our interest is to find the sideband signal outside of the main signal SASE bandwidth, the sideband signal is weak. Such signals could hardly be seen by human eyes on the spectrum 2-D raw images or the integrated 1-D spectrum profile. Therefore, we created software that relies on machine learning to detect such very weak signals from the background noise. This paper introduces this software and discusses its processes.

2 Approach

2.0 Forward

In a Self-Seeded Tapered FEL, the FEL spectrum contains three parts: (1) the strong seeded main frequency with a relative bandwidth on the order of 10^{-3} ; (2) the SASE signal with relative bandwidth on the order of 10^{-1} . Both seeded main frequency and SASE signal are strong with narrow bandwidth. The sideband signal, on the other hand, is a wideband signal and is extremely weak. In order to detect the very weak and wideband sideband, in the software, there are three processes: (1) remove main frequency and SASE; (2) remove outliers; and (3) organize the remaining data into clusters. These clusters can be regarded as sideband. Throughout this paper, we will refer to Figure 1 and Figure 2 often—we will refer to the former as IMG, and the latter, PWR. IMG is the image of the XFEL captured by the camera—its X and Y coordinates are frequency and size, respectively. Each point is a IMG, with its color referencing its power (lighter means higher power). PWR, on the other hand, is the summation of power down IMG's Y axis—the X axis, frequency, is the same.

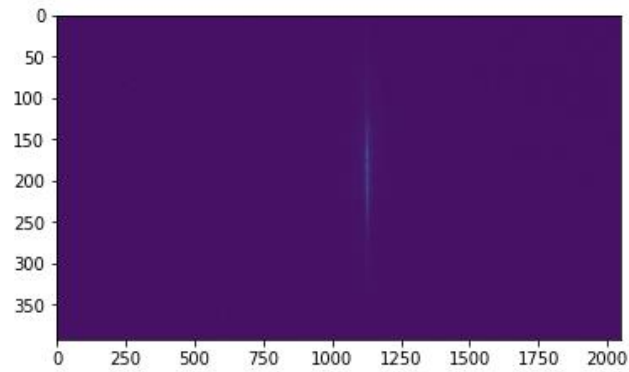


Figure 1: “IMG”

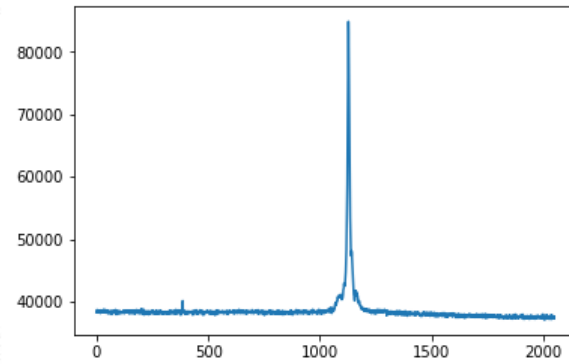


Figure 2: “PWR”

To understand why we must remove the main frequency and SASE, consider the mean shift algorithm. It is a function of both proximity and density. First, it estimates a bandwidth (radius) based on density and proximity of points. Then, from a point (A), it calculates the average point (B) of all points within A’s bandwidth. Next, the algorithm shifts to B and repeats the process, hence the name “mean shift.” The shifting will follow the path of maximum density increase until convergence. The final point of convergence (C) is the centroid of the cluster, and every point that follows a path to C is assigned to C’s cluster.

It follows then that this process will not immediately work on IMG or PWR—neither conveys distance nor density, both of which are necessary for the mean shift algorithm to work. Thus, we converted IMG to a scatter plot. For every IMG that had power over a certain threshold (see section 2.3), we placed that amount of points on their respective coordinates in a new scatter plot, thus allowing the mean shift algorithm to function. Thus, areas with higher power have considerably higher density and considerably lower distance between points.

Recall the bandwidth. Areas with extreme power will influence the bandwidth by making it smaller—this presents a problem when attempting to detect weaker signals, signals that are too spread for a tight bandwidth to cluster appropriately. In this case, the tight bandwidth leads to early convergence and results in an over-abundance of clusters, thus nullifying any attempt to detect weaker, spread out signals. In the same vein, the main frequency and SASE contaminates the bandwidth and interferes with proper sideband detection. Thus, to correctly cluster sideband, we must remove the main frequency and SASE.

2.1 Main Frequency and SASE Removal

We first shifted PWR down the Y axis by subtracting every point by PWR's minimum Y value—this was essential to use gaussian distribution properties. To remove the main frequency and SASE, we used properties of the gaussian curve. Note that the main frequency and the SASE distributions are both normal, and recall that $[u-3\sigma, u+3\sigma]$ composes 99% of the normal distribution. Thus, we used the Full Width at Half Maximum (FWHM) to determine the main frequency's sigma (recall that $\text{FWHM} \approx 2.355\sigma$), then we removed all points in the range $[u-3\sigma, u+3\sigma]$. We repeated this process for the SASE. Note that the main frequency lies within the SASE range, so using SASE boundaries will be sufficient from this point forward.

We note this range [SASE begin, SASE end] and set each IMG in IMG within this range to zero. The result is a set of data with two segments: the portion before the main frequency / SASE gap, and the portion after the main frequency / SASE gap. Observe Figure 3 and 4.

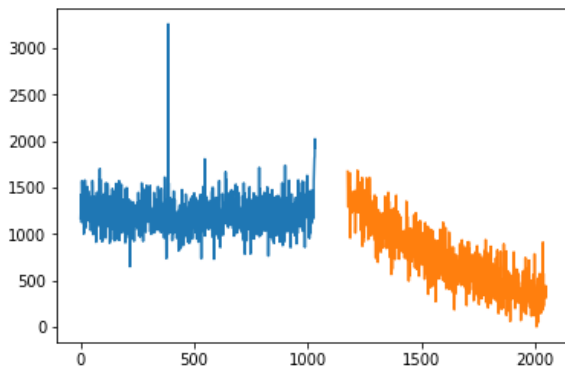


Figure 3: “PWR” after cut

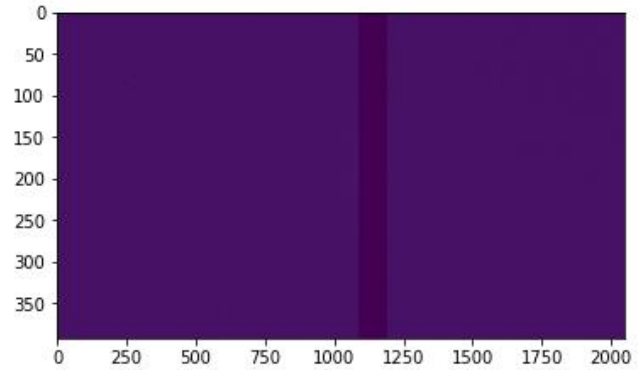


Figure 4: “IMG” after cut

2.2 Outlier Removal

Note the large spike in [Figure 3](#). This is an outlier detectable by eye. However, most outliers are not detectable by eye. These outliers can be caused by a variety of factors, such as a dead IMG on the camera, an escaped electron, etc. The outliers can adversely affect the mean shift results. Therefore, we removed the outliers.

Removing the outliers involved two different graphs, as portrayed by [Figure E](#) and [Figure F](#). First, we fit polynomial curves to each segment of [Figure 3](#) (see [Figure 5](#)). Then, we took the

absolute value of the difference between each real data point and its respective curve prediction and stored them into an array. This array, when plotted as a histogram, has a distinct gaussian distribution ([Figure 6](#)). We noted sigma. We returned to [Figure 5](#) and noted every outlier that exceeds $3 \times \text{sigma}$ distance from its respective curve. We then converted the power of the columns in IMG sharing the X axis of PWR's outliers. They are converted to the average of the neighboring columns. Finally, we take the resulting IMG to the next step. Note IMG is not shown because the changes done via outlier removal are undetectable by eye.

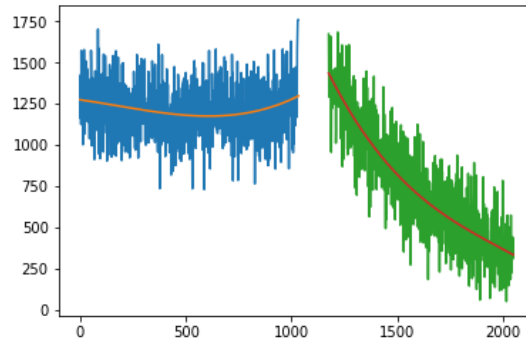


Figure 5: “PWR” post-cut and outlier removal

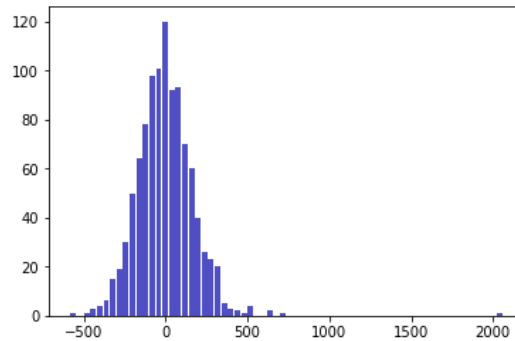


Figure 6: Histogram of of “PWR” after subtracting the fitted value

2.3 Applying Machine Learning

The mean shift algorithm is a function of density and distance, not value; therefore, the IMG would not be sufficient as it were for the algorithm. Thus, we converted the IMG to a usable

format as follows: (1) we observed the power level (P) of each coordinate, (2) we placed P amount of points in the same coordinates on a new graph, effectively creating a density map.

To decrease runtime, we added a filter. If P was less than Filter (F), we did not convert that respective filter. We found that if the filter was too high, it adversely affected the results; conversely, if F was too low, runtime was substantial. We performed a convergence test and found the proper Filter to be 40. After filtering, we then applied the mean shift algorithm and stored the resulting cluster amount of each IMG in an array for further analysis.

3 Results

Figure 7 is a sample sideband for one IMG. Figure 8 is a distribution for a sample of 106 IMGs.

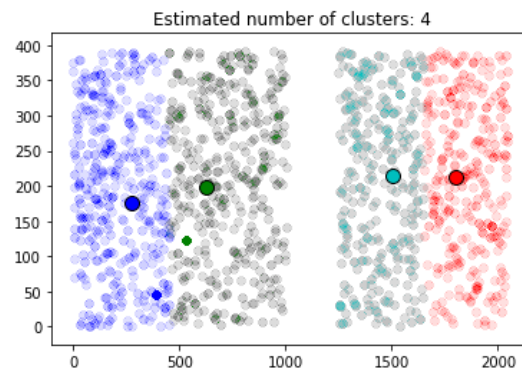


Figure 7: sample sideband for one IMG

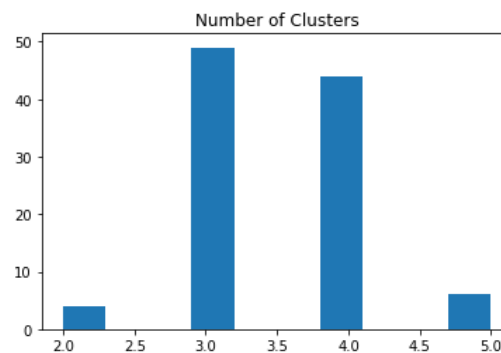


Figure 8: a distribution for a sample of 106 IMGs

4 Discussion and Conclusion

This software can be applied to any frequency data in which possible sideband needs to be isolated and identified. A possible future work is to incorporate this software into a machine that trains itself to suppress sideband.

One limitation of this software is if there is powerful, obvious sideband, it could potentially be counted as outlier and minimized, which would negatively impact the detection of hidden sideband. In this case, the software should be edited so it uses its main frequency removal method on these obvious sideband areas as well.

Another limitation of this software is the main frequency it removes must have a normal distribution. In the case that the main frequency does not have a normal distribution, another main frequency removal process should be used before proceeding to curve smoothing and ultimately machine learning clustering.

Bibliography

- Aquila, A., Barty, A., Bostedt, C., Boutet, S., Carini, G., dePonte, D., . . . Williams, G. J. (2015). The linac coherent light source single particle imaging road map. *Structural Dynamics*, 2(4), 041701.
- Bonifacio, R., Casagrande, F., Ferrario, M., Pierini, P., & Piovella, N. (1988). Hamiltonian model and scaling laws for free-electron-laser amplifiers with tapered wiggler. *Opt. Commun.*, 66, 133.
- Cheng, Y. (1995). Mean Shift, Mode Seeking, and Clustering. *IEEE Transactions on Pattern Analysis and Machine Intelligence*, 17(8), 790.
- Davidson, R. C., & Wurtele, J. S. (1987). Single-particle analysis of the free-electron laser sideband instability for primary electromagnetic wave with constant phase and slowly varying phase. *Phys. Fluids*, 30, 557.
- Emma, C., Fang, K., Wu, J., & Pellegrini, C. (2016). High efficiency, multiterawatt x-ray free electron lasers. *Physical Review Accelerators and Beams*, 19(2), 020705.
- Emma, P., Akre, R., Arthur, J., Bionta, R., Bostedt, C., Bozek, J., . . . Galayda, J. (2010). First lasing and operation of an angstrom-wavelength free-electron laser. *Nature Photonics*, 4, 641.
- Geloni, G., Kocharyan, V., & Saldin, E. (2011). A novel self-seeding scheme for hard X-ray FELs. *Journal of Modern Optics*, 58(16), 1391.

- Hemsing, E., Garcia, B., Huang, Z., Raubenheimer, T., & Xiang, D. (2017). Sensitivity of echo enabled harmonic generation to sinusoidal electron beam energy structure. *Phys. Rev. Accel. Beams*, 20, 060702.
- Isermann, S., & Graham, R. (1992). Suppression of the sideband instability in tapered free-electron lasers. *Phys. Rev. A*, 45, 4050.
- Ishikawa, T., Aoyagi, H., Asaka, T., Asano, Y., Azumi, N., Bizen, T., . . . Kumagai, N. (2012). A compact X-ray free electron laser emitting in the sub-angstrom region. *Nat. Photonics*, 6, 540544.
- Jiao, Y., Wu, J., Cai, Y., Chao, A. W., Fawley, W. M., Frisch, J., . . . Reiche, S. (2012). Modeling and multidimensional optimization of a tapered free electron laser. *Phys. Rev. ST Accel. Beams*, 15, 050704.
- Kroll, N. M., Morton, P. L., & Rosenbluth, M. N. (1981). Free-Electron Lasers with Variable Parameter Wigglers. *IEEE JOURNAL OF QUANTUM ELECTRONICS*, QE-17, 1436.
- Lindberg, R. (2015). *AOP-TN-2015-028*.
- Masud, J., Marshall, T. C., Schlesinger, S. P., Yee, F. G., Fawley, W. M., Scharlemann, E. T., . . . Sternbach, E. J. (1987). Sideband Control in a Millimeter-Wave Free-Electron Laser. *Phys. Rev. Lett.*, 58, 763.
- Pilla, R. P., & Bhattacharjee, A. (1994). Elimination of the sideband instability in variableparameter freeelectron lasers and inverse freeelectron lasers. *Phys. Plasmas*, 1, 390.
- Quimby, D. C. (1988). Sideband generation and mode structure in free-electron lasers. *Proc. SPIE Int. Soc. Opt. Eng.*, 0738, 103.
- Ribic, P. R., Roussel, E., Penn, G., De Ninno, G., Giannessi, L., Penco, G., & Allaria, E. (2017). Echo-enabled harmonic generation studies for the fermi free-electron laser. *Photonics Spectra*, 4, 19.
- Riyopoulos, S. (2000). Sideband suppression in tapered wiggler free electron lasers including thermal spreads. *Phys. Plasmas*, 7, 1586.
- Roussel, E., Ferrari, E., Allaria, E., Penco, G., Mitri, S. D., Veronese, M., . . . Giannessi, L. (2015). Multicolor High-Gain Free-Electron Laser Driven by Seeded Microbunching Instability. *Phys. Rev. Lett.*, 115, 214801.
- Schneidmiller, E. A., & Yurkov, M. V. (2013). Obtaining high degree of circular polarization at x-ray free electron lasers via a reverse undulator taper. *Phys. Rev. ST Accel. Beams*, 16, 110702.
- Sharp, W. M., & Yu, S. S. (1990). Two-dimensional vlasov treatment of free-electron laser sidebands. *Phys. Fluids B*, 2, 581.
- Tokar, R. L., McVey, B. D., & Goldstein, J. C. (1988). Sideband suppression in free electron lasers using a grating rhomb. *IEEE J. Quantum Electron.*, 24, 856.

- Tsai, C.-Y., Wu, J., Yang, C., Yoon, M., & Zhou, G. (2017). Sideband instability analysis based on a one-dimensional high-gain free electron laser model. *Phys. Rev. Accel. Beams*, *20*, 120702.
- Tsai, C.-Y., Wu, J., Yang, C., Yoon, M., & Zhou, G. (2018). Single-pass high-gain tapered free-electron laser with transverse diffraction in the postsaturation regime. *Phys. Rev. Accel. Beams*, *21*, 060702.
- Valentine, K. P. <https://github.com/kpvalentine/SLAC-sideband-detection-ML>. (2018).
- Wu, J., Hu, N., Setiawan, H., Huang, X., Raubenheimer, T., Jiao, Y., . . . Qiang, J. (2017). Multi-dimensional optimization of a terawatt seeded tapered Free Electron Laser with a Multi-Objective Genetic Algorithm. *Nuclear Instruments and Methods in Physics Research A*, *846*, 56.
- Yee, F. G., Masud, J., Marshall, T. C., & Schlesinger, S. P. (1987). Power and sideband studies of a raman FEL. *Nucl. Instrum. Methods Phys. Res., Sect. A*, *259*, 104.
- Zhang, Z., Lindberg, R., Fawley, W. M., Huang, Z., Krzywinski, J., Lutman, A., . . . Marinelli, A. (2016). Microbunching-instability-induced sidebands in a seeded free-electron laser. *Phys. Rev. Accel. Beams*, *19*, 050701.